BNL-223685-2022-JAAM

Reconfigurable perovskite nickelate electronics for artificial intelligence

H. Zhang, Y. Zhu

To be published in "SCIENCE"

February 2022

Condensed Matter Physics and Materials Science Department

Brookhaven National Laboratory

U.S. Department of Energy

USDOE Office of Science (SC), Basic Energy Sciences (BES) (SC-22)

DISCLAIMER

Reconfigurable Perovskite Electronics for Artificial Intelligence

Hai-Tian Zhang[1,†,*], Tae Joon Park[1,†,*], A. N. M. Nafiul Islam[2,†], Dat S. J. Tran[3,†], Sukriti Manna[4,5,†], Qi Wang[1,†], Sandip Mondal[1], Haoming Yu[1], Suvo Banik[4], Shaobo Cheng[6], Hua Zhou[7], Sampath Gamage[8], Sayantan Mahapatra[9], Yimei Zhu[6], Yohannes Abate[8], Nan Jiang[9], Subramanian K.R.S. Sankaranarayanan[4,5], Abhronil Sengupta[2], Christof Teuscher[10] and Shriram Ramanathan[1,*]

[1]School of Materials Engineering, Purdue University, West Lafayette, IN 47907, USA

[2] Department of Electrical Engineering, The Pennsylvania State University, University Park, PA, 16802, USA

[3]Department of Electrical and Computer Engineering, Santa Clara University, Santa Clara, CA 95053, USA

[4]Center for nanoscale materials, Argonne National Laboratory, Argonne, IL 60439, USA

[5]Department of Mechanical and Industrial Engineering, University of Illinois, Chicago, IL 60607, USA

[6]Department of Condensed Matter Physics and Materials Science, Brookhaven National Laboratory, Upton, NY 11973, USA

[7]X-ray Science Division, Advanced Photon Source, Argonne National Laboratory, Lemont, IL 60439, USA

[8]Department of Physics and Astronomy, University of Georgia, Athens, GA 30602, USA

[9]Department of Chemistry, University of Illinois at Chicago, Chicago, Illinois 60607, USA

[10]Department of Electrical and Computer Engineering, Portland State University, Portland, OR, 97207, USA

[†]*These authors contributed equally to this work*
[*]*Electronic mail: htzhang@purdue.edu, park1080@purdue.edu, shriram@purdue.edu*

Neurogenesis and synaptogenesis refer to the synthesis of brain matter, which is essential for information processing, memory, and intelligence. The nerve cells (neurons) and their interconnections (synapses) not only form during the growth of a fetus but continue to evolve,

modify and reconfigure post-birth well-into the young adult stage as noted across birds,(*1, 2*) **animals**(*3*) **and humans**(*4–6*) **and is essential for the continuous learning ability of organisms**(*6, 7*) **and repair of neural circuits following brain injury.**(*8, 9*) **A principal goal of neuromorphic (brain-inspired) computing is to emulate features of intelligence found in nervous systems in electronic hardware.**(*10–13*) **Here, we demonstrate artificial neurogenesis, i.e. on-demand creation of neurons, synapses and memory capacitors within individual post-fabricated perovskite devices that can be simply reconfigured for a specific purpose by single-shot electric pulses. This discovery is enabled via a unique combination of the extreme sensitivity of perovskite nickel oxides to the local distribution of hydrogen ions as well as a vast array of metastable states available for the protons to reside in the host lattice. With experimental data from our memory capacitors, simulation results of a brain-inspired reservoir computing framework show excellent performance comparable to theoretical reservoirs for diverse tasks such as handwritten, spoken digit recognition, and classification of electrocardiogram heartbeat activity. By using the experimental results of our reconfigurable artificial neurons and synapses, we simulate dynamic network grow and show that they outperform static networks by up to 250% accuracy for incremental learning scenarios. The ability to fashion the basic building blocks of brain-inspired computers on-demand opens up the possibility of life-long machine learning.**

The brain is a continuously evolving organ that is remarkably plastic. Plasticity in brains includes the formation of neurons (neurogenesis) as well as synapses (synaptogenesis) that interconnect the neurons to form neural circuits. These processes are crucial from the fetus stage to later developmental stages of the nervous system. Early studies on neurogenesis were focused on the ability of songbirds to develop seasonal song repertoires.(*1*, *2*) Since then, neurogenesis has been noted in adult human brains, which has significance in providing cognitive adaptability,(*6*, *7*) improving the performance in behavioral tasks such as pattern recognition,(*14*) and recovery from brain injury.(*8*, *9*) Neurogenesis and synaptic rewiring via structural plasticity play a crucial role in the formation of memory,(*15*, *16*) and a dynamic brain is therefore essential for life-long learning.

In AI, however, continual learning presents a formidable challenge. Models are generally trained on stationary data distributions and thus when new data is presented incrementally to a neural network, it interferes with the previously learned knowledge, resulting in poor performance, known as catastrophic forgetting,(*17*, *18*) which remains an active field of research.(*19–22*) One of the major approaches to tackle this issue is to actively adapt the structure of the network itself when new data becomes available. Modulating the architecture of the network in response to the input distribution not only allows the network to manage its resources efficiently but also recent discoveries suggest that a dynamic network can show better performance compared to a static network when provided with equal resources.(*23*, *24*) Moreover, as smart edge devices become more integrated into society, they will require the implementation of sophisticated networks in hardware constrained by both chip area and power. Having the ability to reallocate network resources dynamically to perform various tasks in an ever-changing environment will be of fundamental importance. Up to date, neurogenesis in AI networks has been looked at primarily from a software point of view.(*23*, *25*) Having these capabilities in hardware can be game-changing for future computers whose designs are inspired by the intelligence of animal brains.

Here, we show that perovskite nickelates, a class of quantum materials that undergo room temperature electronic phase transitions upon hydrogen doping, enable a versatile, reconfigurable hardware platform for adaptive computing. A single device made from H-doped $NdNiO_3$ for instance, can be electrically reconfigured on-demand to take on either the functionalities of neurons, synapses, and memory capacitors respectively, as described in **Figure 1(a)** and **(b)**. Such versatile tunability is uniquely enabled by the synergistic combination of a vast array of metastable configurations for protons in the perovskite lattice that can also be voltage controlled. While a variety of ionic-electronic switches are being actively explored for neuromorphic computing,(*26–35*) complete reconfiguration of neuromorphic functions has remained elusive. To demonstrate use cases in artificial intelligence, we use the experimental data from our memory capacitors in a Reservoir Computing (RC) framework (**Figure 1(c)**), a brain-inspired machine learning architecture, and simulation results demonstrate excellent performance comparable to theoretical reservoirs. The experimental characteristics of neurons and synapses obtained from the perovskite nickelate devices and their run-time reconfigurability are leveraged to design self-adaptive dynamic Grow-When-Required (GWR) networks (**Figure 1(d))**. Motivated by the cortical data processing in the brain,(*36*, *37*) GWR networks present an unsupervised approach to lifelong learning in real-world scenarios with limited availability of training samples which in turn may have missing or noisy labels. We demonstrate that such networks can exploit the creation and deletion of network nodes on the fly to offer greater representation power and efficiency in comparison to static counterparts.

Results and discussion

Perovskite nickelates (chemical formula $ReNiO_3$ where Re is a rare-earth ion such as Nd) are a class of quantum materials whose electronic properties are mediated by strong electron interactions.(*38–40*) Pristine $NdNiO_3$ is a correlated metal at room temperature. Hydrogen dopants as an electron donor can lead to several orders of magnitude reduction in electrical conductivity by modifying the Ni orbital configuration.(*41*, *42*) Gently re-distributing the hydrogen ions (protons) already doped in the lattice by electric fields can modify the electrical conductivity systematically to generate a multitude of electronic states. As an example, by annealing $NdNiO_3$ (NNO) devices in hydrogen gas (with catalytic electrodes such as Pd or Pt), hydrogen can be doped interstitially into the NNO lattice proximal to the electrode. The hydrogens then donate electrons to the Ni *d* orbitals, which changes the filling state in the NNO *d* band and results in a phase transition with several orders of magnitude change in resistivity.(*41*) (From here on, the hydrogen-doped NNO will be referred as H-NNO for simplicity) A vast array of metastable energy states are available to the protons in the lattice and thus their distribution, local concentration (and thereby function) can be subsequently modulated via electric fields applied to the electrode. We hypothesize that the observed various functional states arise from configurational disorder induced by metastability of H-NNO. To confirm this, we use a reinforcement learning (see **Methods** and **Supplementary Figure 2**) search algorithm interfaced with DFT+U calculations to explore the various metastable H-NNO states (shown in **Figure 2(a)-(d)** and **Supplementary Figure 3**). Their structural diversity is further evident from the principal component analysis (PCA) representation of the sampled metastable configurations in the fingerprint space, see **Figure 2(e)** and **supplementary Figure 4** that describes the PCA analysis for different stoichiometries of H concentration in H-NNO. These high dimensional representations of the configurations are rotationally and translationally invariant and allow us to precisely identify the uniqueness of the sampled configuration. We then sample ~120 low energy metastable H-NNO phases for 1:1 H:Ni stoichiometry. These metastable states differ primarily by the interstitial locations of H within the NNO lattice and energetically vary by ~150 meV/atom with respect to the lowest energy configuration, see **Figure 2(f)**. We next compute the partial density of states (PDOS) of the various metastable H-NNO configurations. From the PDOS plot, we observe that at 1:1 H:Ni stoichiometry, the density of states of spin up electrons splits at Fermi level and opens a gap of ~0.4 eV (**Figure 2(g)**) – the extent of this gap depends on the metastability or the location of the interstitial H (**Supplementary Figure 5**). The PBEsol + 2 computed band gaps of all the metastable configurations of H-NNO are shown in **Figure 2(h),** and the band gap of H-NNO with the lowest configurational energy is shown by the green dotted line. The computed band gap of across all the metastable structures has a mean value of 0.47 eV with a variation of +/- 0.4 eV (min ~0.1 eV and max ~0.9 eV). This suggests that subtle configurational disorder in interstitial H can introduce significant variations in the resistance states that can in turn be exploited for different functions.(*43*) The metastable states and PDOS plots of H-NNO with varying H:Ni ratio are provided in **Supplementary Figure 6**.

To demonstrate reproducible electrical reconfiguration in H-NNO, NNO films were deposited by different methods, i.e. sputtering and atomic layer deposition (ALD), as well as on different substrates, i.e. $LaAlO_3$ and SiO_2/Si, see **Supplementary Figure 7** for structural characterization of pristine NNO films and **Supplementary Figure 8** for device details. First, we describe the capacitive behavior (charge storage) in our devices. Capacitors not only are useful for storing charge in the conventional sense, but are also central for numerous brain-inspired computing architectures. Evolution of memcapacitive loop states in the perovskite nickelate device as a function of hydrogen doping is shown in **Supplementary Figure 9**. With increasing hydrogen doping, the H-NNO film resistance increased and then eventually saturated at ~10^8 Ω, see **Supplementary Figure 9(a)**. To explore the capacitive behaviors of the H-NNO device at different hydrogen doping states, cyclic voltage sweeps were performed, see **Supplementary Figure 9(b-h)**. Pristine and weakly doped perovskite NNO shows linear resistor behavior. At intermediate doping state, capacitive behavior appears. Electrical reconfiguration of the H-NNO device is summarized in **Figure 2(i)-(n)**. By applying positive and negative electric pulses, the resistance state of the device can be modulated carefully, and the programmed resistance states are non-volatile as shown in **Supplementary Figure 10**. The energy barriers associated with proton migration in the NNO lattice has been discussed in **Supplementary Note 1**. At the electronic state (i), cyclic voltage sweep measurements of the nickelate device were performed and linear resistor behavior was observed as shown in **Figure 2(i)**. The electronic state (i) was then switched to electronic state (ii) by applying a single voltage pulse, where an I-V loop appeared, indicating stored energy in the device, as shown in **Figure 2(j)**. Memristive and memcapacitive behaviors were also demonstrated at state (ii), as detailed in **Supplementary Note 2.**

Next, we show the creation of artificial neurons and synapses (that are responsible for information transfer and memory in the brain) from the same device. Spiking neuronal behavior in the H-NNO device was studied at the electronic state (iii) as shown in **Figure 2(k)**. Consecutive electric stimuli were applied to the device and once a critical level was reached, abrupt changes in the device resistance were observed. The non-volatile neuronal response of the nickelate device to electric stimulus depends on both pulse voltage and pulse width as described in **Supplementary Figures 11-12**. A typical spiking probability plot is shown in **Figure 2(l)**, which can be directly implemented in neural networks. We then demonstrate synaptic behavior at electronic state (iv) in the nickelate device by continuous voltage sweeps as shown in **Figure 2(m)**. In **Supplementary Figure 13**, threshold pulse fields were investigated for both high resistance state (HRS, state iii) and low resistance state (LRS, state iv). At LRS, smaller threshold pulse field (V_{th}) is sufficient to modulate the device resistance, which is suitable for analog behavior with gradual resistance changes. However, this analog update of device resistance prohibits the sudden jump in resistance necessary for spiking. At HRS, a much higher V_{th} is required to change the resistance, and it is beneficial for spiking neuronal behavior. Detailed characterization of representative H-NNO devices are presented in **Supplementary Figure 14-18**. Finally, the linear resistor state (v) in **Figure 2 (n)** can be restored by applying a single electric pulse. To demonstrate versatility of the device platform, electrical reconfiguration at different resistance states of H-NNO device is shown in **Supplementary Figure 19**. To summarize, a single device can be reconfigured as resistor, memcapacitor, neuron or synapse by electric pulses.

Nickelate devices with 100 nm gap size were also fabricated to demonstrate scalability, endurance, reproducibility and ultra-low energy consumption as shown in **Supplementary Figures 20-23**. In scaled devices, electrical reconfiguration can be realized with < 10ns electric pulses. The energy cost for a single synaptic update is ~2 fJ, which is comparable with that in the brain (1~100fJ).(*44*, *45*) To demonstrate compatibility with CMOS technology, nickelate devices were fabricated on SiO_2/Si substrates by both sputtering and atomic layer deposition (industrial technique used to grow high quality metal-oxide films for state-of-the-art electronics)(*46*) and data are shown in **Supplementary Figures 24** and **25**.

To showcase applications of the adaptive nickelate hardware, we apply the experimental memristive and memcapacitive behaviors in Reservoir Computing (RC), a brain-inspired machine learning architecture that addresses the issue of training complexity and parameter explosion commonly observed in traditional Recurrent Neural Networks (RNNs) by only adapting a simple output layer. RC explains higher-order cognitive functions and the interaction of short-term memory with other cognitive processes.(*47*) Details can be found in **Supplementary Note 2.** To have a baseline comparison, we evaluated the performance of our H-NNO device in comparison to theoretical models(*48*, *49*) for three different tasks: MNIST, isolated spoken digit recognition, and ventricular heartbeat classification on an electrocardiogram (ECG) dataset. In **Figure 3(a)**, the simulation results show that the H-NNO-based reservoirs achieved better or comparable performances on all three tasks when compared to the two theoretical reservoirs, see **Figure 3(b)-(d)**. For example, when classifying ventricular ectopic heartbeats from the ECG dataset, the H-NNO reservoir improved the simulation time in the training phase. The H-NNO reservoir achieved its final classification much faster at 20,000 training heartbeats, ~80% faster compared to the reservoirs in both theoretical models, see **Figure 3(d)**. Our results illustrate that neuromorphic H-NNO reservoirs can solve complex tasks and match or even outperform theoretical models and elaborated upon in **Supplementary Note 2**.

Having the neuronal and synaptic functionality in a single type of device can enable compact and energy efficient neuromorphic system designs. Discussion on deep neural networks using such perovskite networks is given in **Supplementary Note 3**. Furthermore, the ability to reconfigure devices for multiple neuromorphic functions opens up their innovative use in next generation AI, namely in the emerging domain of dynamic neural networks. The Grow-When-Required (GWR) network is one such example, that creates new nodes and their interconnections according to competitive Hebbian learning. The GWR networks expand on the concept of self-organizing neural networks by adding or removing network nodes in an unsupervised manner to approximate the input space accurately and at times more parsimoniously compared to a static self-organizing map.(*50*) We can compare the dynamic GWR with a static self-organizing network that uses the same Hebbian learning scheme but has a fixed number of nodes, initialized randomly in the beginning. We trained our network on two archetypal datasets used to evaluate performance in literature – MNIST(*51*) and a subset of CUB-200(*52*) to simulate how such a network will perform on-the-fly. For discussion on the datasets and details of the simulation refer to **Methods** and **Supplementary Notes 4**. The GWR network's ability to dynamically respond to changes in the input distribution is visualized in **Figure 4(a)** for MNIST.

For both the datasets and networks, we conducted two sets of simulations using the experimental data from our H-NNO devices– 1) incremental learning – where the network is shown newer classes of data over time and 2) assessing the effect of growing/shrinking compared to static networks– i.e., how efficiently can the GWR represent the input space. **Figure 4(b)-(e)** shows the network's test accuracy and the number of nodes as each new class is trained for both the datasets in the incremental learning scenario. We observe that the dynamic network is able to retain its learned representations much better than the static network, with the final test accuracy being 212% better for MNIST and 250% for CUB-200. By growing its size, the network avoids suffering from catastrophic forgetting and shows only a smooth degradation in performance as the number of classes is increased. Note, the size of the static network was chosen to be equal to the maximum number of nodes that the GWR network required. This ensured that the difference we observe is not due to the size difference of the two networks but rather because of the dynamic network's ability to grow and learn.

We then studied the ability of the GWR network to dynamically change its size to adapt to the input space. Firstly, we assess the networks' ability to grow as the number of classes in the network is increased abruptly (**Figure 4(f)** and **(g))**. Initially, we present the networks with the first half of the total number classes in the datasets and see the GWR grows and saturates in size. Afterwards, when the networks are presented with the entire dataset, the GWR rapidly grows its size to accommodate the change. The static network is not able to do so and thus fails to learn the new data while also suffering degradation in performance in the initial classes. (See **Supplementary Note 4** and **Supplementary Figures 26** and **27** for detailed accuracy results). Overall, the dynamic networks achieve significantly better accuracy on the test set in comparison to the static network, 210% for MNIST and 170% for CUB-200. Next, we demonstrate that the GWR is able to efficiently allocate its resources compared to a large static network. We present the network with all the classes of the dataset at the beginning. After learning has occurred, we remove half the categories and let the GWR network reduce its size and reach an equilibrium number of nodes (**Figure 4(h)** and **(i)**). We find that the GWR is able to retain a similar level of the performance to the large static network (accuracy difference 2-3%) on the subset of interest, and demonstrate higher efficiency through shrinking its size by ~47% for MNIST and ~27% for CUB-200. (See **Supplementary Note 4** and **Supplementary Figures 28** and **29** for detailed accuracy results.)

Conclusions

In conclusion, we have demonstrated artificial neurogenesis, i.e., creation of essential hardware building blocks for brain-inspired computers on-demand within a single device platform. Dynamic deep learning networks simulated with the experimentally measured characteristics of the nickelate devices consistently outperform static counterparts. The results showcase the potential of reconfigurable perovskite quantum electronic devices for emerging computing paradigms and AI machines. Additionally, semiconductor technology compatible atomic layer deposition on silicon platforms and room temperature operation of test chips can further enable widespread adoption of perovskite quantum materials into mainstream integrated circuit manufacturing.

Acknowledgements: We would like to sincerely thank Professor Alexander Chubykin at the Purdue Institute for Integrative Neuroscience for valuable discussions on neurogenesis; synaptogenesis and repair of neural circuits**.** We would like to sincerely thank Professor Karin Rabe (Rutgers University), Dr. Subhasish Mandal (Rutgers University) and Dr. Michele Kotiuga (EPFL) for valuable discussions on mechanisms leading to capacitive behavior in hydrogen-doped nickelates. The analysis of the synaptic properties and related measurements were supported by Energy Frontier Research Centers (EFRC) funded by the U.S. Department of Energy (DOE), Office of Science, Basic Energy Sciences (BES), under Award DE-SC0019273. The fabrication and pulsed field measurements were supported by AFOSR FA9550-19-1-0351 and ARO W911NF-19-2-0237 respectively. A. N. M. N. I. and A. S.'s research was funded in part by the National Science Foundation (BCS #2031632 and CCF #1955815). Use of the Center for Nanoscale Materials and Advanced Photon Source, both Office of Science user facilities, was supported by the U.S. Department of Energy, Office of Science, Office of Basic Energy Sciences, under Contract No. DE-AC02-06CH11357. This research used resources of the National Energy Research Scientific Computing Center (NERSC), a U.S. Department of Energy Office of Science User Facility located at Lawrence Berkeley National Laboratory, operated under Contract No. DE-AC02-05CH11231. This material is based upon work supported by the U.S. Department of Energy, Office of Science, Office of Basic Energy Sciences Data, Artificial Intelligence and Machine Learning at DOE Scientific User Facilities program. We thank Alex Hexemer for providing us computational time on NERSC and useful discussions on the workflow development for predicting the metastable phases of materials. This work at BNL was supported by DOE-BES, Materials Sciences and Engineering Division under Contract No. DE-SC0012704. This research used resources of the Advanced Photon Source, a U.S. Department of Energy (DOE) Office of Science User Facility, operated for the DOE Office of Science by Argonne National Laboratory under Contract No. DE-AC02-06CH11357. Extraordinary facility operations were supported in part by the DOE Office of Science through the National Virtual Biotechnology Laboratory, a consortium of DOE national laboratories focused on the response to COVID-19, with funding provided by the Coronavirus CARES Act. S. G. and Y.A. acknowledge support from the Air Force Office of Scientific Research (AFOSR), Grant No. FA9559-16-1-0172 and National Science Foundation (NSF), Grant No. 1904097. S. M. and N. J. acknowledge support from the National Science Foundation (CHE-1944796).

Author contributions: H.-T. Z., T. J. P., and S. R. conceived the study. T. J. P. and H.-T. Z. grew the nickelate films. Q. W. fabricated the devices. H.-T. Z., T. J. P. and S. M. conducted electrical measurements. H. Y. and T. J. P. performed XRD characterization. H. Z. performed synchrotron X-ray characterization. S. C. and Y. Z. performed TEM chacterization. S. G. and Y. A. carried out Scattering-type scanning near-field optical microscopy. S. M. and N. J. performed near-field tip-enhanced Raman measurements. A. N. M. N. I. and A. S. performed the all-perovskite deep network and the GWR neural network simulations and analysis. D. S. J. T. performed the RC simulation and C. T. co-led the discussions of these results. S. M., S. B., and S. K. R. S. S. carried out all the reinforcement learning based search and the *ab-initio* calculations. H.-T. Z., T. J. P. and S. R. organized the manuscript. All authors participated in discussing the results and providing various sections and comments for the paper.

Competing interests: The authors declare no competing interests.

Data and materials availability: The data that support the findings of this study are available from the corresponding author upon reasonable request.

Code availability: The reinforcement learning search for metastable states is implemented in the CASTING (Continuous Action Space Tree search for INverse desiGn) framework and is available from the authors *via* proposal submission system at the Center for Nanoscale Materials at Argonne National Laboratory.

References

1. S. A. Goldman, F. Nottebohm, Neuronal production, migration, and differentiation in a vocal control nucleus of the adult female canary brain. *Proc. Natl. Acad. Sci. U. S. A.* **80**, 2390–2394 (1983).

2. F. Nottebohm, From bird song to neurogenesis. *Sci. Am.* **260**, 74–79 (1989).

3. H. van Praag, G. Kempermann, F. H. Gage, Neural consequences of enviromental enrichment. *Nat. Rev. Neurosci.* **1**, 191–198 (2000).

4. F. H. Gage, Mammalian neural stem cells. *Science (80-.).* **287**, 1433–1438 (2000).

5. T. L. Spires-Jones, C. W. Ritchie, A brain boost to fight Alzheimer's disease. *Science (80-.).* **361**, 975–976 (2018).

6. A. Ernst, K. Alkass, S. Bernard, M. Salehpour, S. Perl, J. Tisdale, G. Possnert, H. Druid, J. Frisén, Neurogenesis in the striatum of the adult human brain. *Cell*. **156**, 1072–1083 (2014).

7. H. Shani-Narkiss, A. Vinograd, I. D. Landau, G. Tasaka, N. Yayon, S. Terletsky, M. Groysman, I. Maor, H. Sompolinsky, A. Mizrahi, Young adult-born neurons improve odor coding by mitral cells. *Nat. Commun.* **11**, 5867 (2020).

8. D. M. Arzate, L. Covarrubias, Adult Neurogenesis in the Context of Brain Repair and Functional Relevance. *Stem Cells Dev.* **29**, 544–554 (2020).

9. W. Tai, X. M. Xu, C. L. Zhang, Regeneration Through in vivo Cell Fate Reprogramming for Neural Repair. *Front. Cell. Neurosci.* **14**, 107 (2020).

10. D. Marković, A. Mizrahi, D. Querlioz, J. Grollier, Physics for neuromorphic computing. *Nat. Rev. Phys.* **2**, 499–510 (2020).

11. J. D. Kendall, S. Kumar, The building blocks of a brain-inspired computer. *Appl. Phys. Rev.* **7**, 11305 (2020).

12. C. S. Thakur, J. L. Molin, G. Cauwenberghs, G. Indiveri, K. Kumar, N. Qiao, J. Schemmel, R. Wang, E. Chicca, J. Olson Hasler, J. Seo, S. Yu, Y. Cao, A. van Schaik, R. Etienne-Cummings, Large-Scale Neuromorphic Spiking Array Processors: A Quest to Mimic the Brain. *Front. Neurosci.* **12**, 891 (2018).

13. T. Dalgaty, E. Vianello, B. De Salvo, J. Casas, Insect-inspired neuromorphic computing. *Curr. Opin. Insect Sci.* **30**, 59–66 (2018).

14. G. li Ming, H. Song, Adult Neurogenesis in the Mammalian Brain: Significant Answers and Significant Questions. *Neuron*. **70**, 687–702 (2011).

15. A. Barnea, V. Pravosudov, Birds as a model to study adult neurogenesis: bridging evolutionary, comparative and neuroethological approaches. *Eur. J. Neurosci.* **34**, 884–907 (2011).

16. A. Knoblauch, in *The Rewiring Brain*, A. van Ooyen, M. Butz-Ostendorf, Eds. (Academic Press, San Diego, 2017), pp. 361–386.

17. J. L. McClelland, B. L. McNaughton, R. C. O'Reilly, Why there are complementary learning systems in the hippocampus and neocortex: Insights from the successes and failures of connectionist models of learning and memory. *Psychol. Rev.* **102** (1995), pp. 419–457.

18. M. McCloskey, N. J. Cohen, Catastrophic Interference in Connectionist Networks: The Sequential Learning Problem. *Psychol. Learn. Motiv.* **24**, 109–165 (1989).

19. X. Li, Y. Zhou, T. Wu, R. Socher, C. Xiong, in *Proceedings of the 36th International Conference on Machine Learning*, K. Chaudhuri, R. Salakhutdinov, Eds. (PMLR, 2019), vol. 97 of *Proceedings of Machine Learning Research*, pp. 3925–3934.

20. J. Kirkpatrick, R. Pascanu, N. Rabinowitz, J. Veness, G. Desjardins, A. A. Rusu, K. Milan, J. Quan, T. Ramalho, A. Grabska-Barwinska, D. Hassabis, C. Clopath, D. Kumaran, R. Hadsell, Overcoming catastrophic forgetting in neural networks. *Proc. Natl. Acad. Sci.* **114**, 3521–3526 (2017).

21. G. I. Parisi, R. Kemker, J. L. Part, C. Kanan, S. Wermter, Continual lifelong learning with neural networks: A review. *Neural Networks*. **113**, 54–71 (2019).

22. R. Kemker, M. McClure, A. Abitino, T. Hayes, C. Kanan, Measuring catastrophic forgetting in neural networks. *Proc. AAAI Conf. Artif. Intell.* **32**, 3390–3398 (2018).

23. S. Parisi, German I. and Ji, Xu and Wermter, *NIPS'18 Work. Contin. Learn.*, in press.

24. K. O. Stanley, J. Clune, J. Lehman, R. Miikkulainen, Designing neural networks through neuroevolution. *Nat. Mach. Intell.* **1**, 24–35 (2019).

25. T. J. Draelos, N. E. Miner, C. C. Lamb, J. A. Cox, C. M. Vineyard, K. D. Carlson, W. M. Severa, C. D. James, J. B. Aimone, in *2017 International Joint Conference on Neural Networks (IJCNN)* (2017), pp. 526–533.

26. X. Zhu, D. Li, X. Liang, W. D. Lu, Ionic modulation and ionic coupling effects in MoS2 devices for neuromorphic computing. *Nat. Mater.* **18**, 141–148 (2019).

27. L. Q. Zhu, C. J. Wan, L. Q. Guo, Y. Shi, Q. Wan, Artificial synapse network on inorganic proton conductor for neuromorphic systems. *Nat. Commun.* **5**, 3158 (2014).

28. N. K. Upadhyay, H. Jiang, Z. Wang, S. Asapu, Q. Xia, J. Joshua Yang, Emerging Memory Devices for Neuromorphic Computing. *Adv. Mater. Technol.* **0**, 1800589 (2019).

29. Y. Wang, K.-M. Kang, M. Kim, H.-S. Lee, R. Waser, D. Wouters, R. Dittmann, J. J. Yang, H.-H. Park, Mott-transition-based RRAM. *Mater. Today*. **28**, 63–80 (2019).

30. E. J. Fuller, S. T. Keene, A. Melianas, Z. Wang, S. Agarwal, Y. Li, Y. Tuchman, C. D. James, M. J. Marinella, J. J. Yang, A. Salleo, A. A. Talin, Parallel programming of an ionic floating-gate memory array for scalable neuromorphic computing. *Science (80-.).* **364**, 570–574 (2019).

31. T. Ohno, T. Hasegawa, T. Tsuruoka, K. Terabe, J. K. Gimzewski, M. Aono, Short-term plasticity and long-term potentiation mimicked in single inorganic synapses. *Nat. Mater.* **10**, 591–595 (2011).

32. R. A. John, F. Liu, N. A. Chien, M. R. Kulkarni, C. Zhu, Q. Fu, A. Basu, Z. Liu, N. Mathews, Synergistic gating of electro-iono-photoactive 2D chalcogenide neuristors: coexistence of hebbian and homeostatic synaptic metaplasticity. *Adv. Mater.* **30**, 1800220 (2018).

33. R. A. John, J. Acharya, C. Zhu, A. Surendran, S. K. Bose, A. Chaturvedi, N. Tiwari, Y. Gao, Y. He, K. K. Zhang, Optogenetics inspired transition metal dichalcogenide neuristors for in-memory deep recurrent neural networks. *Nat. Commun.* **11**, 1–9 (2020).

34. W. Yi, K. K. Tsang, S. K. Lam, X. Bai, J. A. Crowell, E. A. Flores, Biological plausibility and stochasticity in scalable VO 2 active memristor neurons. *Nat. Commun.* **9**, 1–10 (2018).

35. J. H. Yoon, Z. Wang, K. M. Kim, H. Wu, V. Ravichandran, Q. Xia, C. S. Hwang, J. J. Yang, An artificial nociceptor based on a diffusive memristor. *Nat. Commun.* **9**, 1–9 (2018).

36. D. J. Felleman, D. C. Van Essen, Distributed hierarchical processing in the primate cerebral cortex. *Cereb. Cortex*. **1**, 1–47 (1991).

37. R. Malach, I. Levy, U. Hasson, The topography of high-order human object areas. *Trends Cogn. Sci.* **6**, 176–184 (2002).

38. G. Catalan, Progress in perovskite nickelate research. *Phase Transitions*. **81**, 729–749 (2008).

39. S. Catalano, M. Gibert, J. Fowlie, J. Íñiguez, J.-M. Triscone, J. Kreisel, Rare-earth nickelates RNiO3: thin films and heterostructures. *Reports Prog. Phys.* **81**, 046501 (2018).

40. Q. Guo, S. Farokhipoor, C. Magén, F. Rivadulla, B. Noheda, Tunable resistivity exponents in the metallic phase of epitaxial nickelates. *Nat. Commun.* **11**, 2949 (2020).

41. J. Shi, Y. Zhou, S. Ramanathan, Colossal resistance switching and band gap modulation in a perovskite nickelate by electron doping. *Nat. Commun.* **5**, 1–9 (2014).

42. C. Oh, S. Heo, H. M. Jang, J. Son, Correlated memory resistor in epitaxial NdNiO3 heterostructures with asymmetrical proton concentration. *Appl. Phys. Lett.* **108**, 122106 (2016).

43. M. Kotiuga, K. M. Rabe, *arXiv*, in press.

44. Y. Van De Burgt, E. Lubberman, E. J. Fuller, S. T. Keene, G. C. Faria, S. Agarwal, M. J. Marinella, A. Alec Talin, A. Salleo, A non-volatile organic electrochemical device as a low-voltage artificial synapse for neuromorphic computing. *Nat. Mater.* **16**, 414–418 (2017).

45. Y. Liu, J. Zhong, E. Li, H. Yang, X. Wang, D. Lai, H. Chen, T. Guo, Self-powered artificial synapses actuated by triboelectric nanogenerator. *Nano Energy*. **60**, 377–384 (2019).

46. H. H. Sønsteby, E. Skaar, Ø. S. Fjellvåg, J. E. Bratvold, H. Fjellvåg, O. Nilsen, A foundation for complex oxide electronics -low temperature perovskite epitaxy. *Nat. Commun.* **11**, 2872 (2020).

47. M. Rigotti, D. Ben Dayan Rubin, X.-J. Wang, S. Fusi, Internal Representation of Task Rules by Recurrent Dynamics: The Importance of the Diversity of Neural Responses. *Front. Comput. Neurosci.* **4**, 24 (2010).

48. M. G. A. Mohamed, H. Kim, T. W. Cho, Modeling of Memristive and Memcapacitive Behaviors in Metal-Oxide Junctions. *Sci. World J.* **2015**, 910126 (2015).

49. D. Biolek, M. Di Ventra, Y. V. Pershin, Reliable SPICE simulations of memristors, memcapacitors and meminductors. *Radioengineering*. **22**, 945–968 (2013).

50. S. Marsland, J. Shapiro, U. Nehmzow, A self-organising network that grows when required. *Neural networks*. **15**, 1041–1058 (2002).

51. Y. LeCun, The MNIST database of handwritten digits. *http://yann.lecun. com/exdb/mnist/* (1998).

52. C. Wah, S. Branson, P. Welinder, P. Perona, S. Belongie, *Comput. Neural Syst. Tech. Rep.*, in press.

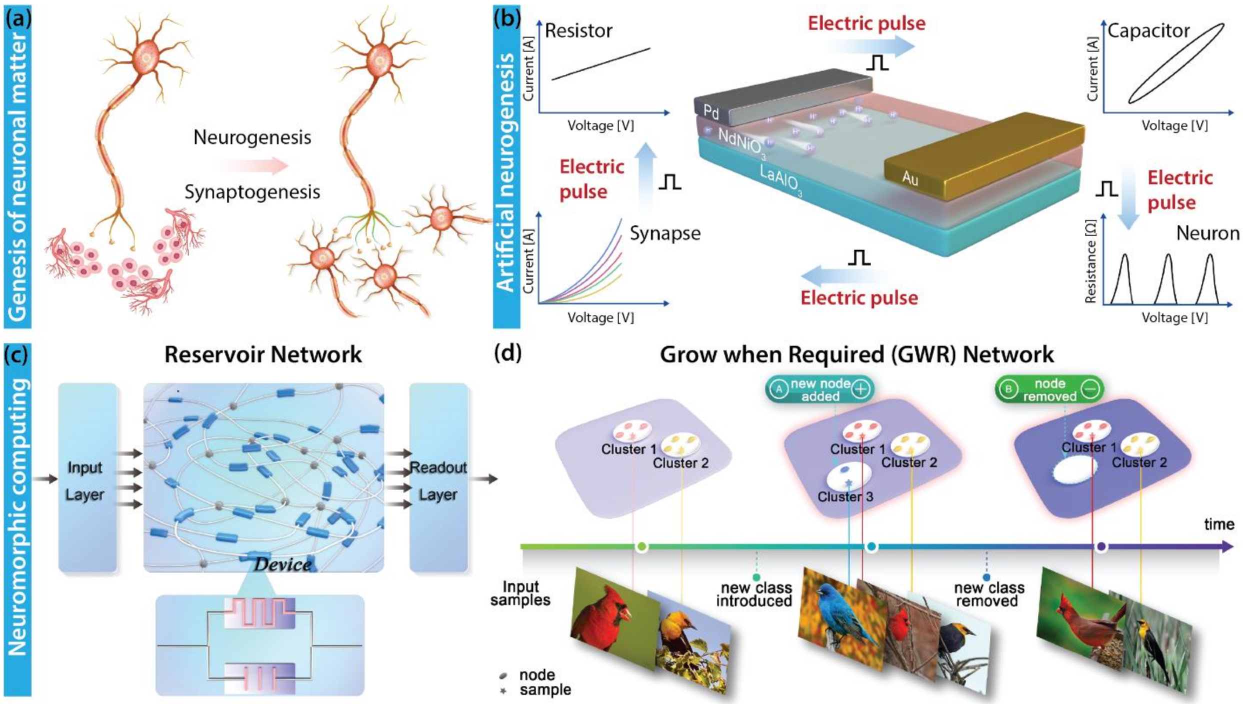

Figure 1. Biological vs Electronic neurogenesis. (a) Schematic of biological neurogenesis, generation/modification of neurons (neurogenesis) and synapses (synaptogenesis), and their connections in neural circuits at various stages of life is essential for the life-long learning ability of organisms and recovery from brain injury. This serves as an inspiration for neuromorphic computers. **(b)** Schematic of hydrogen-doped perovskite nickelate as a versatile reconfigurable platform that can be electrically transformed between neurons, synapses, and memory capacitors to enable adaptive neuromorphic computing. By applying electric pulses, the hydrogen ions in the nickelate lattice can occupy metastable states and enable distinct functionalities. **(c)** Schematic of a generic Reservoir Computing (RC) framework. An input layer distributes the signals into the reservoir, which projects the inputs into a high-dimensional space. This is commonly done by relying on non-linear reservoir dynamics. Here, the reservoir is built randomly from programmable devices with memory. No training happens in the reservoir, only the linear readout layer is trained by a simple gradient descent algorithm. The role of the readout layer is to map the high-dimensional dynamics of the reservoir to the output states. **(d)** Schematic of Grow When Required (GWR) Networks. As the network is shown various classes of data it maps high dimensional data to a low dimensional map field to perform clustering on the classes. When a new class is added to the input stream, the network can detect the novel input and grow in size by adding network nodes to accommodate it. Such incremental learning is not possible for traditional neural networks, which suffer from catastrophic forgetting. Additionally, if any of the classes do not appear in the input stream for a long time, the corresponding nodes become inactive thereby saving resources.

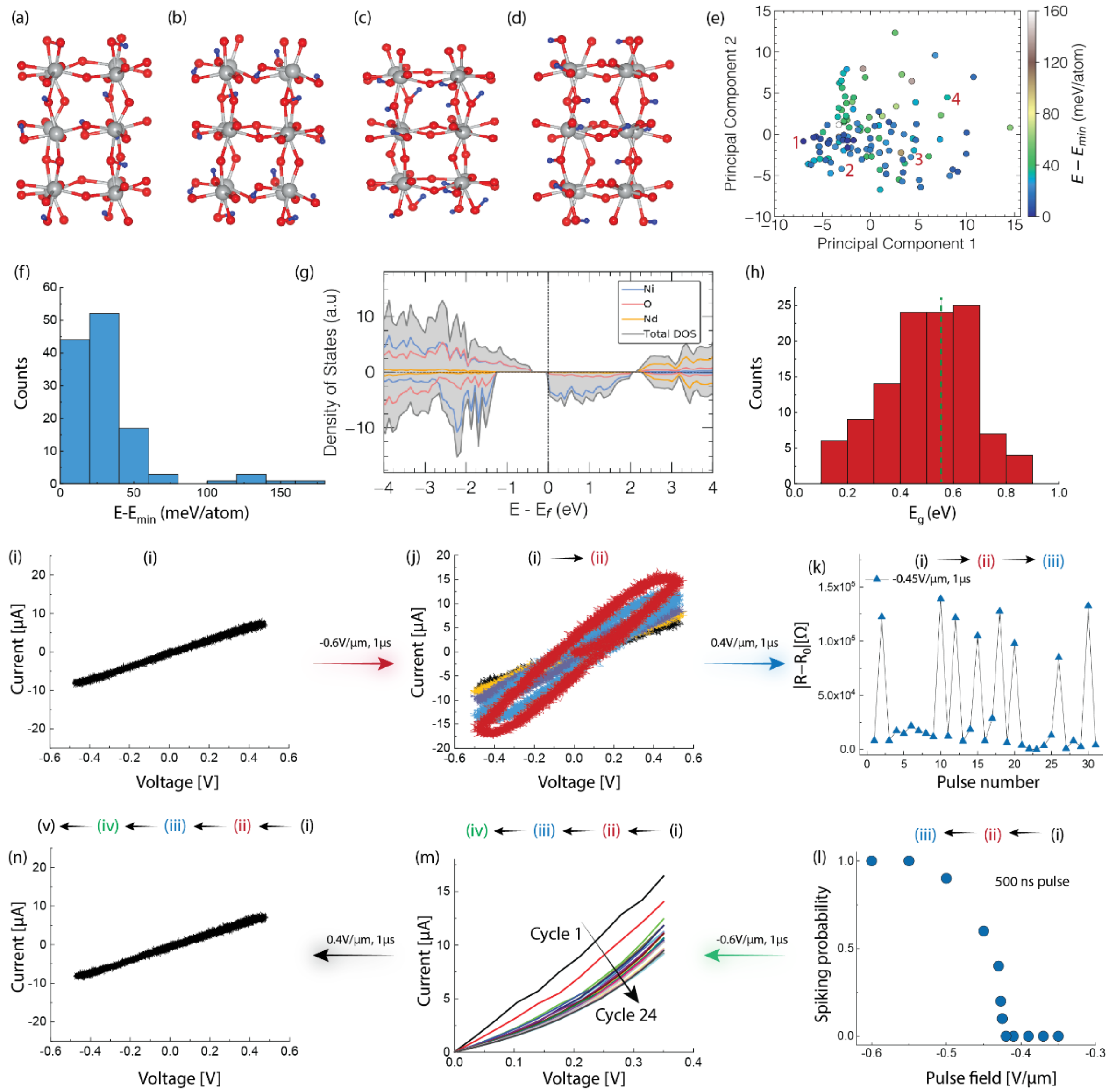

Figure 2. A single perovskite device can be electrically reconfigured to perform essential functions in a neuromorphic computer. (a)-(d) Representative metastable structures showing various H configurations in NNO lattice. Blue solid balls represent various metastable interstitial positions of H within the NNO lattice. Red and grey solid balls represent for O and Ni atoms, respectively. For clarity, Nd atoms are not shown. **(e)** A principal component analysis (PCA) representation of configurational diversity in the sampled phases as represented in the SOAP fingerprint space. Representative metastable H-NNO structures in (a)-(d) are marked as 1-4. Color bar shows the energy variation with respect to the energetically lowest (E_{min}) configuration sampled by the RL algorithm. Each point in the PCA plot represents a principal component of 1160 dimensional representation of each metastable phases computed using the SOAP fingerprinting technique. **(f)** Energy distribution of the sampled metastable states determined via RL search algorithm. **(g)** Calculated DOS of 1:1 H doped NNO showing gap opening. The PDOS of pristine and H-NNO at different H stoichiometries are provided in Supplementary Information.

(h) Estimated band gap distribution across the various metastable configurations. The green dash line in the band gap distribution plot is the band gap of lowest energy H doped NNO structure. A variation of ~0.9 eV in the band gap is observed for H-NNO depending on the metastable configuration. **(i)** Nickelate device as a *linear resistor* under cyclic voltage sweep. **(j)** Nickelate device as a *capacitor* under cyclic voltage sweep, the appearance of I-V loop indicates stored energy in the device. I-V loops of different sizes can be generated by applying pulse fields (ii). Complete details can be found in **Supplementary Note 2**. **(k)** Nickelate device as a *spiking neuron* (iii). Resistance changes of the nickelate device were monitored in response to consecutive electric pulses (-0.45 V/μm for 1 μs). After the spike fires, the resistance of the device was restored to the original state by applying reset voltage pulse (+0.45 V/μm for 1 μs). **(l)** Spiking probability of nickelate device as a function of pulse field, showing stochastic behavior. **(m)** Nickelate device as a *synapse*. I-V curves of nickelate devices were measured under continuous voltage sweeps. The resistance of the device increases continuously, showing analog synaptic updates. **(n)** Resetting nickelate device back to initial *linear resistor* state.

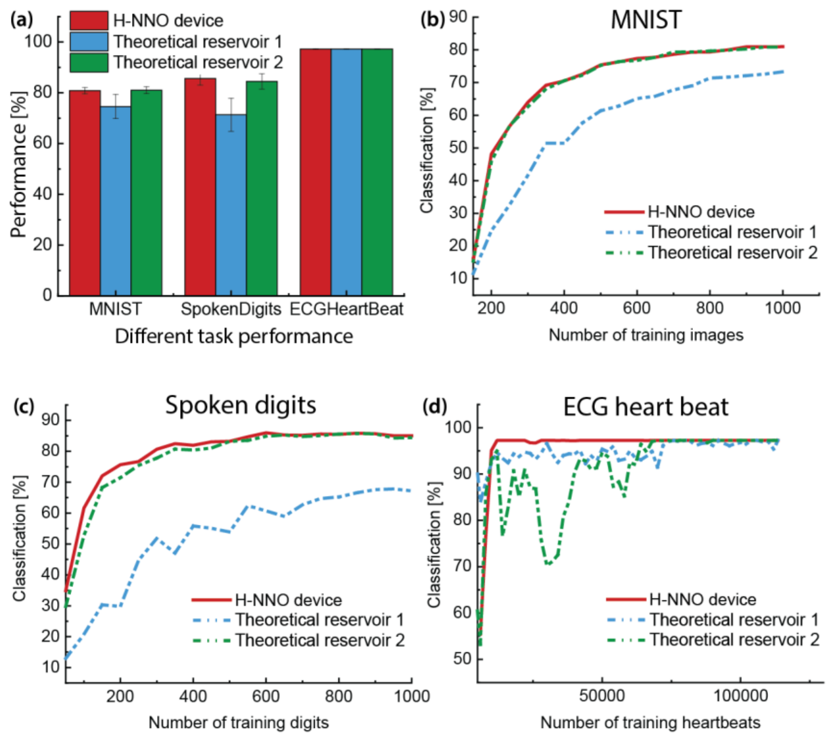

Figure 3. Reservoir computing with experimental data measured from nickelate devices. (a) The simulation results of reservoirs with H-NNO devices, compared to theoretical models of reservoirs, demonstrate that a large and random network of H-NNO devices can function as a hardware platform for neuromorphic computing in solving complex tasks. The results were the average of simulating a sample size of 100 reservoirs with similar hyperparameters for each reservoir type. **(b)-(d)** In training for a simple task (MNIST) (b), the H-NNO reservoir improved its training classification with an increasing number of images, similar to its theoretical counterparts. However, in training for more complex tasks, such as recognizing spoken digits (c), the classification of the H-NNO reservoirs converged faster. Particularly in training for classifying ventricular ectopic heartbeats in ECG (d), the H-NNO reservoir achieved its final classification with 80% fewer training heartbeats, compared to the theoretical reservoirs.

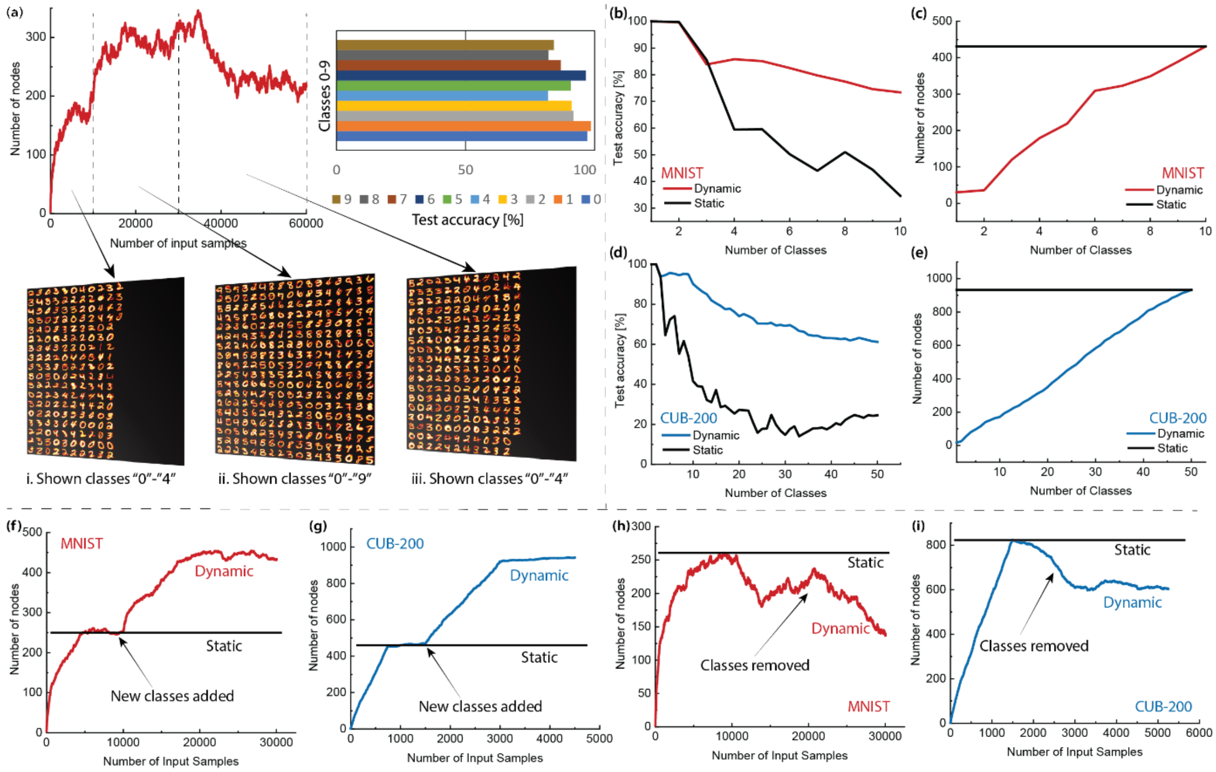

Figure 4. Dynamic grow-when-required computing with experimental characteristics measured from nickelate devices. (a) Visualization of grow-when-required (GWR) network's ability to dynamically respond to changes in the input distribution over time for the MNIST dataset. Firstly, we showed the network 10,000 input samples from the first five classes ('0'- '4') of MNIST dataset. The network can grow and learn the representation as seen in (i). Next, the network is trained on 20,000 samples from all the 10 classes of MNIST. Due to the addition of new classes the network grows in size and accommodates them as seen in (ii). The accuracy over all the classes is shown in the bar chart in the top right corner. Finally, we again change the input class distribution by only showing the network the classes '0'- '4'. We observe that the network can gradually shrink its size as nodes associated with the last five classes slowly become inactive and are removed from the network as seen in (iii). Here the digits are the learnt representations of the nodes whereas each unit of the black region indicates an unused/inactive node in the network. **(b)-(e)** Network performance for incremental learning of classes. (b) Test accuracy for MNIST as the number of classes is incrementally increased from 1 to 10, (c) Number of nodes as the number of classes is increased for MNIST. (d) Test accuracy for the 50 classes of CUB-200 as the number of classes is incrementally increased from 1 to 50. (e) number of nodes as the number of classes is increased for CUB-200. **(f-i)** Assessing the effect of dynamically changing size of GWR compared to static network with fixed number of nodes. (f, g) The GWRs achieve 51.6% better accuracy on MNIST and 41.3% better accuracy on CUB-200 compared to static networks that were not allowed to grow beyond the size of the dynamic network prior to learning the new classes. (h, i) We observe similar performance on the classes that are available in both the networks, however, the dynamic network

achieves this with almost half (~47.3%) the number of resources/nodes for MNIST and ~27% fewer nodes for the 50 classes of CUB-200 compared to the static networks.

<u>List of Supplementary material</u>

Methods section

Supplementary Figure 1. Laser spot calibration for tip-enhanced Raman spectroscopy (TERS) measurement.

Supplementary Figure 2. Monte Carlo Tree Search.

Supplementary Figure 3. Possible interstitial H sites in NNO lattice.

Supplementary Figure 4. Principal component analysis for different H doping levels.

Supplementary Figure 5. Different metastable configurations sampled for 1:1 H:NNO stoichiometry using reinforcement learning technique.

Supplementary Figure 6. Effect of doping concentration on phase transition in H-NNO.

Supplementary Figure 7. Characterization of pristine $NdNiO_3$ film on $LaAlO_3$.

Supplementary Figure 8. Electrically reconfigurable nickelate devices on various platforms.

Supplementary Figure 9. Hydrogen doping conditions and the evolution of the I-V loop.

Supplementary Figure 10. Retention of multiple resistance states in nickelate devices.

Supplementary Figure 11. Emergence of neuronal spiking behaviors under different pulse amplitude and pulse widths.

Supplementary Figure 12. Non-volatile neuronal behavior.

Supplementary Figure 13. Threshold pulse field (V_{th}) at different resistance states.

Supplementary Figure 14. Room-temperature confocal Raman scattering analysis of four samples namely pristine, heavily doped NNO/LAO, H-NNO/LAO at LRS, and H-NNO/LAO at HRS.

Supplementary Figure 15. Near-field Raman (TERS) experiment of pristine, heavily doped NNO/Si, H-NNO/Si at LRS, and at HRS in a scanning tunneling microscope setup.

Supplementary Figure 16. s-SNOM imaging of H-NNO devices at different resistance states.

Supplementary Figure 17. Control measurement for s-SNOM imaging of different H-NNO samples.

Supplementary Figure 18. Temperature dependent electrical transport properties of the nickelate device at different resistance states.

Supplementary Figure 19. Electrical reconfiguration of the nickelate device at different resistance states.

Supplementary Figure 20. Sub-10 ns voltage pulses can enable reconfiguration in scaled nickelate devices.

Supplementary Figure 21. Endurance measurement of a representative nickelate device.

Supplementary Figure 22. Analysis of switching ratios in different nickelate devices.

Supplementary Figure 23. Energy consumption estimation of nickelate devices.

Supplementary Figure 24. Electrical reconfiguration in sputtering-grown nickelate device on SiO_2/Si platform.

Supplementary Figure 25. Electrical reconfiguration in ALD grown nickelate device on SiO_2/Si platform.

Supplementary Figure 26. Comparison of accuracy between the dynamic GWR network and the static self-organizing map for training on MNIST.

Supplementary Figure 27. Comparison of accuracy between the dynamic GWR network and the static self-organizing map for training on randomly selected 50 classes of the CUB-200 dataset.

Supplementary Figure 28. Comparison of accuracy and hardware resource utilization between the dynamic GWR network and the static self-organizing map on MNIST.

Supplementary Figure 29. Comparison of accuracy and hardware resource utilization between the dynamic GWR network and the static self-organizing map for training on randomly selected 50 classes of the CUB-200 dataset.

Supplementary Figure 30. Reservoir computing framework.

Supplementary Note 1. Details on Proton Migration Pathways and Barriers for Proton Migration

Supplementary Note 2. Details on the Reservoir Computing Framework

Supplementary Note 3. On-chip learning simulation utilizing experimental data from metastable phases in hydrogen-doped nickelates

Supplementary Note 4. Details on the Grow when Required (GWR) computing